Doppler Lidar Measurements of Vertical Velocity Spectra in the Convective Planetary Boundary Layer

Marie Lothon, Donald H Lenschow, Shane D. Mayor

Doppler Lidar Measurements of Vertical Velocity Spectra in the Convective Planetary Boundary Layer

Marie Lothon · Donald H. Lenschow · Shane D. Mayor

Abstract We utilized a Doppler lidar to measure spectra of vertical velocity w from 390 m above the surface to the top of the daytime convective boundary layer (CBL). The high resolution 2 μm wavelength Doppler lidar developed by the NOAA Environmental Technology Laboratory was used to detect the mean radial velocity of aerosol particles. It operated continuously during the daytime in the zenith-pointing mode for several days in summer 1996 during the Lidars-in-Flat-Terrain experiment over level farmland in central Illinois, U.S.A. The temporal resolution of the lidar was about 1 s, and the range-gate resolution was about 30 m. The vertical cross-sections were used to calculate spectra as a function of height with unprecedented vertical resolution throughout much of the CBL, and, in general, we find continuity of the spectral peaks throughout the depth of the CBL. We compare the observed spectra with previous formulations based on both measurements and numerical simulations, and discuss the considerable differences, both on an averaged and a case-by-case basis. We fit the observed spectra to a model that takes into account the wavelength of the spectral peak and the curvature of the spectra across the transition from low wavenumbers to the inertial subrange. The curvature generally is as large or larger than the von Kármán spectra. There is large case-to-case variability, some of which can be linked to the mean structure of the CBL, especially the mean wind and the convective instability. We also find a large case-to-case variability in our estimates of normalized turbulent kinetic energy dissipation deduced from the spectra, likely due for the most part to a varying ratio of entrainment flux to surface flux. Finally, we find a relatively larger contribution to the low wavenumber region of the spectra

M. Lothon (✉)
Centre de Recherches Atmosphériques, 8 route de Lannemezan, 65300 Campistrous, France
e-mail: lotm@aero.obs-mip.fr

M. Lothon
Laboratoire d'Aérologie - CNRS UMR 5560, Université de Toulouse, Toulouse, France

D. H. Lenschow
National Center for Atmospheric Research, Boulder, CO, USA

S. D. Mayor
California State University, Chico, CA, USA

in cases with smaller shear across the capping inversion, and suggest that this may be due partly to gravity waves in the inversion and overlying free atmosphere.

Keywords Convective boundary layer · Doppler lidar · Turbulence · Vertical velocity spectra

1 Introduction

There are many observations of one-dimensional spectra from in situ sensors in the atmospheric boundary layer, but for the most part, these observations are at a few discrete levels from towers within the surface layer (e.g. Kaimal et al. 1972; Katul and Chu 1998; Mann 1994), or from tethered balloons or tall towers in the mixed layer (Kaimal et al. 1976, 1982), or from aircraft that are not simultaneous in time (e.g. Kaimal et al. 1982). As a result, we have a general understanding of the shapes of component spectra as well as cospectra between velocity components and between a velocity component and a scalar, but little information about how the spectra vary with height z, and how well spectral features are correlated as a function of height.

Recent developments in remote sensing technology now allow us to obtain simultaneous measurements of radial velocity throughout the convective boundary layer (CBL). Banakh and Smalikho (1999) used a continuous wave CO_2 Doppler lidar to estimate the turbulent kinetic energy (TKE) dissipation rate in the surface layer from measurements of Doppler spectral width, structure functions, and spectra. Here we report on measurements of the spectra of vertical air velocity w throughout the CBL from $z \simeq 390\,\mathrm{m}$ to near the CBL top ($z = z_i$) with the NOAA High-Resolution Doppler Lidar (HRDL) (Grund et al. 2001). The data were collected during the Lidars in Flat Terrain (LIFT) experiment (Cohn et al. 1998), with HRDL deployed at the surface in a vertically-pointed mode in a region of nearly level farmland in central Illinois, U.S.A. during July 1996. Previously, these data were used by Lothon et al. (2006) in a study of integral scales and two-point turbulence statistics in the CBL. Further details on the instrumentation, experimental setting, meteorological conditions, and supporting measurements are given by Cohn et al. (1998) and Lothon et al. (2006). Angevine et al. (1998) have summarized the concurrent Flatland Boundary Layer experiment, which shared instruments and had complementary objectives.

The HRDL generates coherent infrared pulses at $2.0218\,\mu\mathrm{m}$ wavelength that are transmitted and received by a 0.2-m telescope at a pulse repetition rate of $200\,\mathrm{s}^{-1}$. During LIFT, the laser generated 0.8 mJ pulses with a radial resolution of 30 m (Grund et al. 2001), and a minimum range (dead-zone) of about 390 m. Typically, the lidar was able to "see" several kilometres horizontally and, at the zenith, was always able to see through the top of the CBL. Changes in aerosol scattering led us to vary the number of pulses averaged together, and thus the temporal resolution (from one to a few seconds) on a daily basis.

Although the HRDL was used in various scanning modes during LIFT, a majority of the observations (110 out of over 160 h) were with the laser beam pointing vertically, since a major focus of LIFT was to examine the vertical structure of w in a CBL. This takes advantage of the lidar's capability to obtain range-resolved radial measurements, from which a two-dimensional field of w can be obtained by use of Taylor's hypothesis; that is by assuming that the field of turbulence is "frozen" as it is advected past the lidar.

Here we show results from 11 LIFT cases with useful vertical HRDL data and differing CBL scaling variables (mean wind, CBL depth, and stability), compare the observed w spectra with previous analytical formulations, and discuss the differences.

2 Mean Structure of the CBL

Table 1 summarizes the mean characteristics of the CBL for each case over the selected time period (about 3–4 h approximately centred on midday) that was chosen for analysis. The periods were selected on the basis of data continuity and quality, and stationarity of the CBL. On most of the days, fair-weather cumulus formed by late morning, but some days showed absolutely no cloud. The cloud fraction χ above the lidar was estimated using a threshold on the HRDL backscatter. Two cases had a maximum of about 4/8; all other cases had less clouds. The weather was hot and humid with rain on 17 and 18 August (but not during the observations).

Profiles of the horizontal mean wind U were obtained from the wind profiler located at Sadorus, IL, about 5 km from the HRDL. The mean potential temperature and water vapour mixing ratio were estimated from radiosonde soundings nearest in time to the selected periods, about 5 km from the HRDL. The area surrounding all these sites is flat and contains a similar patchwork of maize and soybean fields. Therefore we assume that all the sites have the same lower boundary conditions.

The CBL top at $z = z_i$ was estimated from the height at which the variance of the backscatter is maximum. This assumes that $z = z_i$ is a demarcation between a particulate-laden CBL and a relatively clean free troposphere, or between layers of differing aerosol. The lidar backscatter gradient has been commonly used to detect the CBL top inversion (Wilczak et al. 1996; White et al. 1999; Hageli et al. 2000; Martucci et al. 2007; Emeis et al. 2008). Lammert and Boesenberg (2006) show that a common method based on the detection of a large local vertical gradient of backscatter, which gives high resolution estimates of z_i, is improved by an average estimate of z_i using the backscatter variance over 1-h samples. They identified unequivocally the correct estimate of z_i based on the gradient method. Here we use the maximum of backscatter variance over the 3 to 4 h period used for each case to obtain average estimates of z_i. The profiles of backscatter variance show a very well defined maximum (not shown); secondary peaks may be observed in some cases (2, 6 and 21 August), but the absolute maximum is always pronounced, and usually at the lowest altitude (for 10 out of the 11 cases).

We also considered, but rejected, a method based on the height at which the Doppler velocity variance over 1-min segments first exceeded $0.7\,\mathrm{m^2\,s^{-2}}$ over a height increment of 30 m. That is, when the aerosol backscatter first became too weak to provide a measurable velocity and the signal was dominated by noise. The average estimate was then calculated by averaging the 1-min interval series of z_i. This method did not work for one case (20 August), where two layers with similar aerosols occurred so that w was measured in both, while the backscatter method identified the correct height. Although an overlying aerosol layer was also observed during 4 and 21 August (less clear and less deep), it did not result in such a large difference between the two z_i estimates. The velocity method locally identified the cloud base when fair-weather cumulus was growing out of the CBL top, but averaged over the period, the method gave estimates of z_i that lay between cloud base and cloud top. The velocity method can also give erroneous z_i estimates if gravity waves exist in the residual layer, and gave estimates of z_i that were usually equal to or larger than the estimates from the backscatter method.

The estimates of the averaged z_i shown in Table 1 compare well with independent estimates from the nearby wind profilers and with the analyses of Grimsdell and Angevine (1998), Cohn and Angevine (2000), and Grimsdell and Angevine (2002). Values of z_i range from 1000 to 1800 m over our 11 cases. Note that the estimates based on the profiler data were obtained from the maximum of the structure coefficient of the refractive index over height.

Table 1 Mean characteristics of the 11 LIFT cases considered here

Date of 1996	z_i (m)	U ($\mathrm{m\,s^{-1}}$)	θ_{v_m} (K)	r_{v_m} ($\mathrm{g\,kg^{-1}}$)	w_* ($\mathrm{m\,s^{-1}}$)	u_* ($\mathrm{m\,s^{-1}}$)	$\Delta\theta_v$ (K)	ΔU ($\mathrm{m\,s^{-1}}$)	γ ($\mathrm{K\,km^{-1}}$)	ζ	χ	l_w/z_i	λ_w/z_i	A
2 Aug	1350	3.0	299.8	9.8	1.50	0.16	1.16	1.0	4.7	346	0.47	0.24	1.78	0.37
4 Aug	1230	5.2	302.9	10.9	1.17	0.35	/	1.8	2.0	15	0.26	0.17	1.52	0.53
5 Aug	1140	8.6	306.7	14.7	1.32	0.52	1.86	5.8	2.4	6	0.28	0.23	1.10	0.13
6 Aug	1170	7.8	307.7	13.1	1.28	0.46	1.16	1.0	5.9	8	0.20	1.52	3.61	0.39
7 Aug	1110	5.6	308.7	15.6	1.23	0.39	0.35	2.2	1.8	13	0.28	0.39	2.72	0.36
10 Aug	1650	2.2	299.6	8.3	1.51	0.39	2.32	2.9	7.6	205	0.21	0.31	1.70	0.39
12 Aug	1410	4.8	300.8	10.7	1.46	0.19	1.16	1.1	2.6	30	0.41	0.39	3.14	0.47
16 Aug	1350	2.2	298.8	8.2	1.62	0.34	4.88	4.1	1.6	233	0.17	0.23	1.66	0.48
19 Aug	1200	7.2	304.1	11.8	1.19	0.19	3.95	2.9	1.0	8	0.21	0.31	1.88	0.17
20 Aug	930	6.8	305.5	14.8	1.13	0.43	1.63	3.1	1.2	8	0.05	0.31	1.95	0.75
21 Aug	1020	3.4	305.6	11.5	1.11	0.26	0.7	0.9	1.3	32	0.13	0.38	2.63	0.75

θ_{v_m} and r_{v_m} are the mean virtual potential temperature and water vapour mixing ratio in the mixed layer, w_* is the convective velocity scale, u_* is the friction velocity, $\Delta\theta_v$ and $\Delta U = \sqrt{\Delta u^2 + \Delta v^2}$ are jumps across the inversion, γ is the lapse rate above the CBL, $\zeta = -z_i/L$, where L is the Obukhov length, χ is the cloud fraction, and l_w and λ_w are respectively the observed along-wind (transverse) integral scale and the wavelength λ_w at which the w energy density spectrum reaches its maximum, both evaluated at $z_i/2$ and normalized by z_i in the table. Finally, A is the ratio of entrainment flux to surface flux estimated from the normalized dissipation rate profiles. "/" indicates that $\Delta\theta_v$ was too small to be estimated

In Table 1, ΔU, $\Delta\theta_v$, and γ, where $\Delta(\ )$ refers to the jump across the inversion, characterize the entrainment zone and the stability of the free troposphere above, based on wind profiler and radiosonde measurements. The cases range from no shear to significant shear, and from low to moderate mean wind speeds.

We also calculated the convective velocity scale w_* and the friction velocity u_*, which are used for scaling the spectra and dissipation of TKE, and for estimating the Obukhov length L and the stability parameter $\zeta = -z_i/L$. The surface fluxes were obtained from three Flux-PAM systems (Militzer et al. 1995) deployed during the Flatland experiment (Angevine et al. 1998), all about 5 km from the lidar. Two stations were located at the centres of adjacent 65 ha corn and soybean fields, south-west of the HRDL, while the third was in a corn field, north-west of the lidar. A single Applied Technology K sonic anemometer was used at each of the three sites, and its height was periodically adjusted to be about 3 m above the canopy; the averaging time interval for flux estimates was 30 min. We weighted the flux contributions from soybeans (station 3) and corn (stations 1 and 2) equally, which is the approximate distribution of the two crops in the area (Militzer et al. 1995).

Table 1 also displays the length scales that are discussed later in conjunction with the w spectra: the along-wind integral scale l_w and the wavelength λ_w of the maximum in the power spectrum multiplied by wavenumber. Here, l_w is the characteristic scale over which the vertical velocity is significantly correlated with itself (Lenschow and Stankov 1986); thus it represents a characteristic size of the individual eddies. In addition, λ_w is the characteristic scale of the turbulence energy production, which is more related to the distance between thermals in the CBL.

3 Model of Vertical Velocity Spectra

While the spectra have a fairly robust dependence on height within the surface layer (Kaimal et al. 1972), their evolution with height in the mixed layer is less well documented and less robust because of possible effects of processes at the CBL top, such as entrainment and waves.

Kristensen et al. (1989, hereafter KLKC) postulate a general kinematic spectral model for an anisotropic horizontally homogeneous vertical velocity field:

$$\frac{S(k)}{\sigma_w^2} = \frac{l_w}{2\pi} \frac{1 + \frac{8}{3}\left(\frac{l_w k}{a(\mu)}\right)^{2\mu}}{\left\{1 + \left(\frac{l_w k}{a(\mu)}\right)^{2\mu}\right\}^{5/(6\mu)+1}}, \tag{1}$$

where

$$a(\mu) = \pi \frac{\mu\Gamma\left(\frac{5}{6\mu}\right)}{\Gamma\left(\frac{1}{2\mu}\right)\Gamma\left(\frac{1}{3\mu}\right)}, \tag{2}$$

k is wavenumber in the mean wind direction, μ governs the curvature of the spectrum across the transition from zero to $-5/3$ slope, and Γ is the gamma function. Larger values of μ give a sharper transition (increasing curvature) between the inertial subrange and the low wavenumber zero-slope spectral region. The relationship between λ_w and l_w in this model is given by

$$\lambda_w = \left\{ \frac{5}{3}\sqrt{\mu^2 + \frac{6}{5}\mu + 1} - \left(\frac{5}{3}\mu + 1\right) \right\}^{1/(2\mu)} \frac{2\pi}{a(\mu)} l_w. \tag{3}$$

According to this model, the standard deviation can be expressed as

$$\sigma_w^3 = a(\mu)^{-5/2} \left(\frac{\pi\alpha}{2}\right)^{3/2} \epsilon l_w, \tag{4}$$

where $\alpha = 0.52$ is the empirically-determined Kolmogorov constant for the longitudinal velocity component (Hogstrom 1996) and ϵ is the TKE dissipation rate, related to the inertial subrange of the transverse velocity spectrum by

$$S_w(k) = \frac{4}{3}\alpha\epsilon k^{-5/3}. \tag{5}$$

Substituting (3) into (4) we have:

$$\sigma_w^3 = b(\mu)\lambda_w \epsilon, \tag{6}$$

where

$$b(\mu) = \left(\frac{\pi}{32}\right)^{1/2} \left(\frac{\alpha}{a(\mu)}\right)^{3/2} \left\{ \frac{5}{3}\sqrt{\mu^2 + \frac{6}{5}\mu + 1} - \left(\frac{5}{3}\mu + 1\right) \right\}^{-1/(2\mu)}, \tag{7}$$

which links dissipation, variance and the spectral maximum wavelength.

Kaimal et al. (1972) proposed a spectral model for the surface layer based on the Kansas surface layer (tower) measurements and for the mixed layer based on the Minnesota tethered balloon w measurements (Kaimal et al. 1976). The KLKC model gives the Kaimal et al. (1976) spectrum for $\mu = 0.5$, and the widely used Kàrmàn (1948) w spectrum for $\mu = 1$.

Højstrup (1982) utilized those measurements to develop a more generalized model of the w spectra as a function of stability from neutral to very unstable, and from close to the ground up to about $z_* \equiv z/z_i = 0.5$:

$$\frac{kS(k)}{u_*^2} = F(k, z_*) \frac{0.95\, kz_i}{2\pi \left(1 + \frac{kz_i}{\pi}\right)^{5/3}} \zeta^{2/3} + \frac{1}{\pi} \frac{kz_i z_*}{1 + 5.3 \left(\frac{kz_i z_*}{2\pi}\right)^{5/3}} (1 - z_*)^2, \tag{8}$$

where

$$F(k, z_*) = \left(\frac{\left(\frac{kz_i}{2\pi} z_*\right)^2 + (0.3 z_*)^2}{\left(\frac{kz_i}{2\pi} z_*\right)^2 + 0.15^2} \right)^{1/2}. \tag{9}$$

4 Observed Spectra

For each case, the spectra were calculated over the entire 3 to 4 h time series at each range. Figure 1 shows the spectra normalized with the square of the convective velocity w_*, for 6 out of the 11 cases considered in our study. The spectra show considerable variability over the cases, with differing shapes and variation with height.

Usually the spectral energy decreases with height, and the locations of the peaks and valleys show little change with height. Some cases have a decrease in energy with height in the inertial subrange (5, 6, 7, 12, 19, 20 August) and others show energy decreasing with

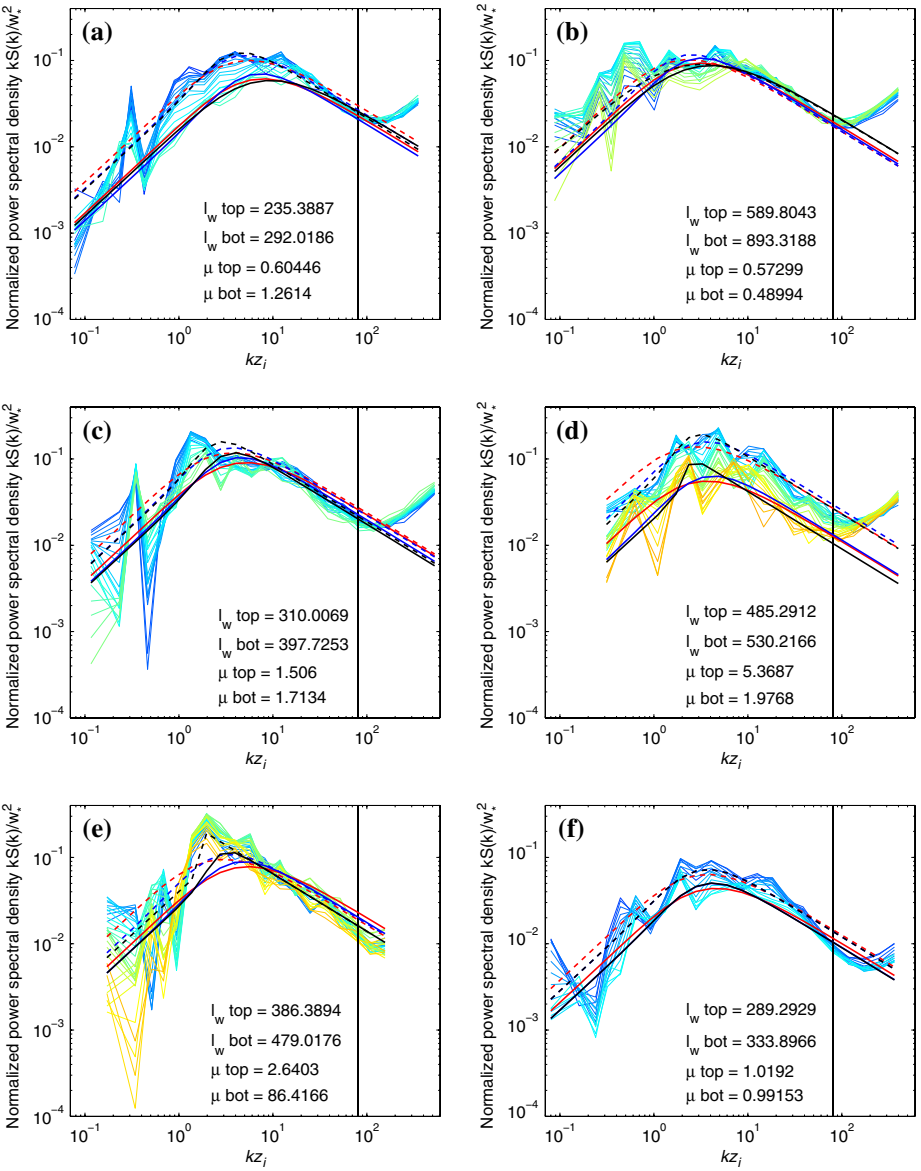

Fig. 1 Normalized spectral density of w multiplied by wavenumber ($kS(k)/w_*^2$) as a function of kz_i for 6 days in August 1996: (**a**) 5, (**b**) 6, (**c**) 7, (**d**) 10, (**e**) 12, (**f**) 20 August. Levels vary from about $0.25z_i$ (*dark blue*) to about $0.9z_i$ (*yellow to orange*) every 30 m. The *smooth red*, *blue lines* and *black lines* are the modeled spectra given in Eq. 1 for respectively $\mu = 0.5$, $\mu = 1$ and varying μ (best fit). They are plotted for the highest (*solid*) and lowest (*dashed*) levels observed

height for all kz_i (2, 4, 10, 16, 21 August). Four cases out of 11 show a variation of spectral energy with height that depends to a large extent on the wavenumber (5, 6, 19 and 20 August), with much smaller variation in the inertial subrange than at smaller wavenumbers. For all other cases the shape of the spectra changes little with height, but the spectral energy does

vary smoothly with height. The cases 5, 6, 19 and 20 August are those with wind speed $>6\,\mathrm{m\,s^{-1}}$. Also note that the days 7 and 12 August have an intermediate behaviour between these two classes, and also have intermediate wind speeds.

We compare the observed spectra to the KLKC model with l_w determined from a least-squares fit to the observed spectra and for different values of μ: (i) $\mu = 0.5$ (Kaimal spectrum, see KLKC Equation (75)), (ii) $\mu = 1$ (von Kàrmàn spectrum), and (iii) μ that gives the best least-squares fit to the observed spectra. In this latter case, μ varies with height and from case to case, as does l_w for all situations. The least-squares fit is limited to $kz_i < 80$ to avoid the noise contribution at large wavenumbers. The modelled spectra in Fig. 1 are plotted at the highest and lowest heights where the velocity spectrum can be measured, while the observed spectra are shown over the whole probed CBL depth with a varying colour scale.

Most of the time, the spectra have a sharper peak than the Kaimal spectrum and even often sharper than von Kàrmàn; that is, μ is often >1. August 6 is the only case where the Kaimal spectrum fits better at all levels (Fig. 1b), due to an additional peak at a lower wavenumber than the usual energy-containing scales, and which reduces curvature in the transition region. For this case $\zeta < 25$, which is a criterion for the occurrence of sub-mesoscale longitudinal rolls (Weckwerth 1999). For August 12, 16 and 19, the modelled spectra do not fit very well, because of energy contributions at relatively large scales and a precipitous fall at still larger scales.

Figure 2 shows the vertical profiles of the μ estimates that give the best fits and the corresponding regression coefficient r. In this figure, data points for $\mu > 8$ are not plotted, because large values of μ produce a triangular bump at the peak that is not observed. This means however that the observed spectra typically have a sharper peak than the previous models. Most of the time, μ decreases with height from the lower CBL up to about $0.7\ z_i$, i.e. the spectra become flatter with increasing height. For example, the spectra for 5 August are close to the von Kàrmàn model in the lower part of the CBL, and close to the Kaimal model in the upper part (Fig. 1a). Days 20 and 21 August show an increase of μ in a thin layer within the CBL, but have μ constant otherwise. Except in this 100-m deep layer, the spectra for 20 August are close to the von Kàrmàn model. The particular case of 6 August has a nearly constant $\mu \simeq 0.5$ over the entire height range. There is a grouping of many cases to a value of around $\mu = 1$ at $z_* = 0.7$.

Cases of large mean wind speed have smaller μ (5, 6, 19, 20 August), and in general, μ decreases with increasing mean wind speed. This can be seen in Fig. 3a, which shows the minimum of μ over height as a function of the mean wind speed. This could be due to the larger sample obtained with larger wind speeds, although the 19 August case has a smaller r than the other high wind cases. We did not find a clear link between clouds or rolls and either r or μ. A link with μ would be difficult to bring out, due to the uncertainty of μ for spectra with sharp peaks and an unusual shape (Fig. 2b). However, we do find a link between the height of minimum μ and the cloud fraction (Fig. 3b), so the larger the cloud fraction, the higher the level at which the flattest spectrum occurs. This is likely due to low wavenumber contributions to the spectrum from cloud activity.

In Fig. 4, we compare the observed normalized $kS(k)/u_*^2$ spectra to the Højstrup (1982) model for the 11 cases at $z_* = 0.35$. The Højstrup (1982) model spectrum is also displayed for each value of ζ. We find that the observed spectra generally show smaller amplitude than predicted by this model, although they vary with ζ as the model predicts, with higher energy for larger ζ. For most of the cases at small kz_i, the spectra decrease faster than predicted for decreasing kz_i. Furthermore, the energy at small kz_i often decreases with height, unlike the predicted spectrum. We find that the sum of the error squared between the modelled and

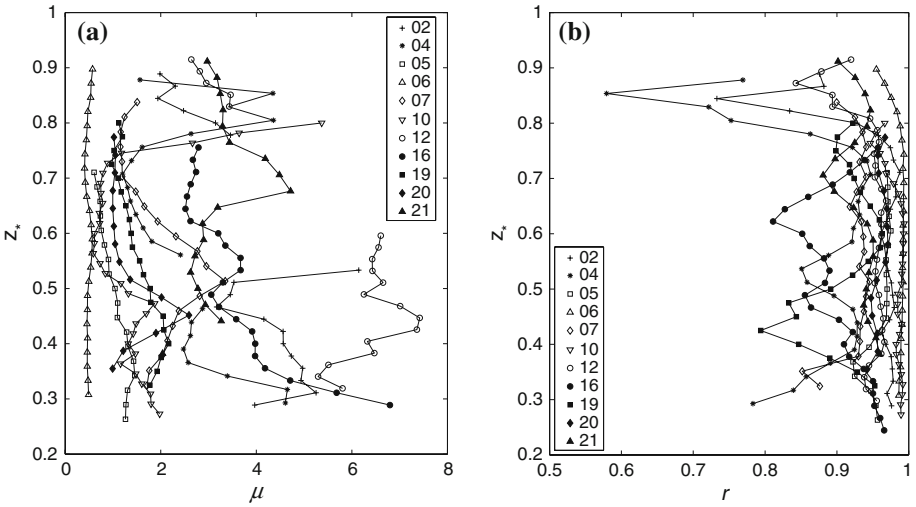

Fig. 2 **a** Profiles of μ obtained by least-squares fit on the observed spectra; **b** profiles of the regression coefficient r. Each *symbol* represents one case

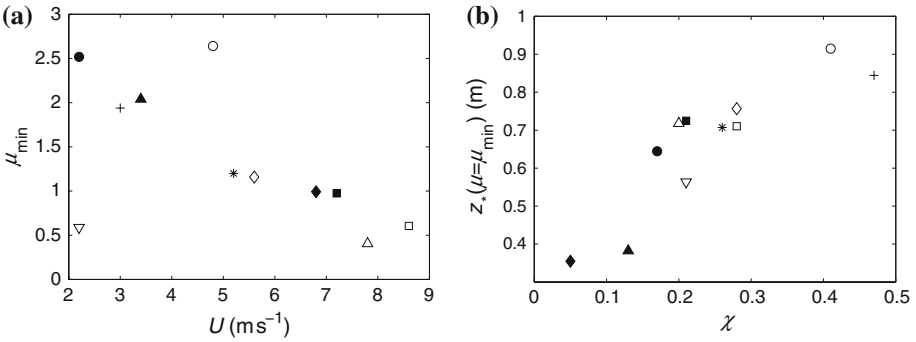

Fig. 3 **a** Minimum of μ over height as a function of the mean wind speed within the CBL; **b** Height where μ is minimum as a function of the cloud fraction. *Symbols* for cases are the same as in Fig. 2

the observed spectra increases with height, especially for $z_* > 0.5$ (not shown). However, this is consistent with Højstrup (1982) who states that the model is meant to apply only for $z_* < 0.5$.

5 Observed Characteristic Length Scales

Vertical profiles of λ_w and l_w normalized by z_i are shown in Fig. 5, with l_w obtained from the best fit to the KLKC model (Eq. 1) and λ_w obtained from l_w using Eq. (3).

The vertical profiles of λ_w (Fig. 5a) are compared with the relationship found by Caughey and Palmer (1979) for the region $0.1 < z_* < 1$:

$$\frac{\lambda_w}{z_i} = 1.8\left(1 - e^{-4z_*} - 0.0003\, e^{8z_*}\right). \tag{10}$$

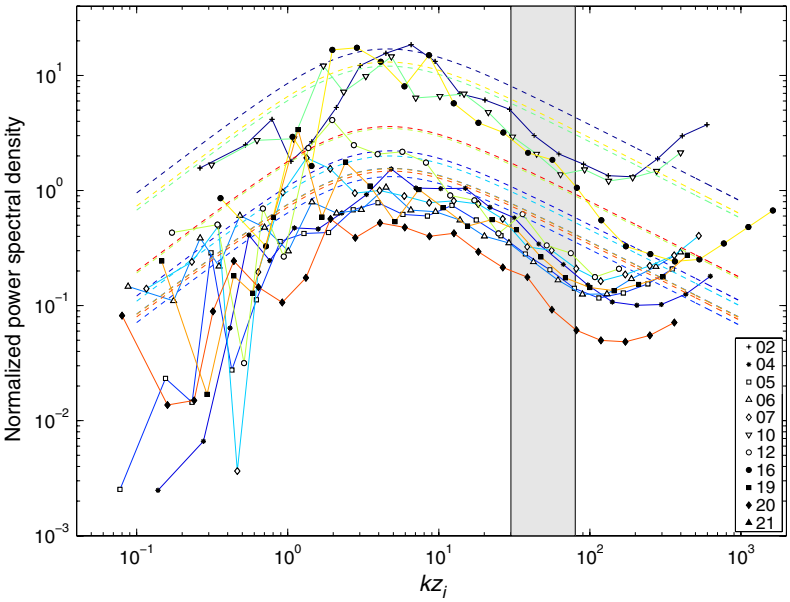

Fig. 4 Normalized spectral density of w multiplied by wavenumber $kS(k)/u_*^2$ as a function of kz_i at $z_* = 0.35$ for the 11 cases. Højstrup (1982) model spectra (depending on ζ) are displayed in each case, with a *dashed line* of same colour. The shaded area indicates the range of the dissipation rate is calculated

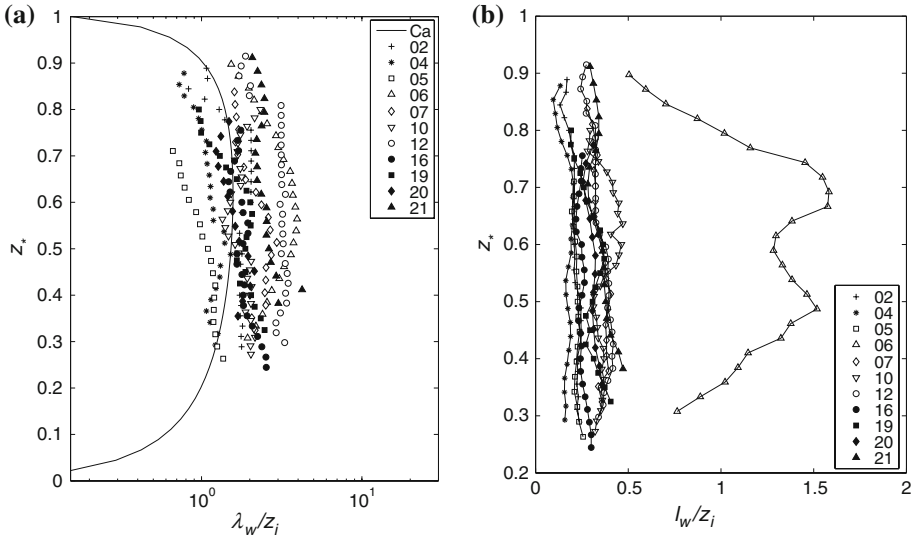

Fig. 5 **a** Profiles of the wavelength λ_w of maximum spectral density of w, normalized by z_i for the 11 cases. *Solid line* is the profile found by Caughey and Palmer (1979) (Eq. 10); **b** profiles of normalized along-wind integral scales for the 11 cases

Five cases show profiles of λ_w/z_i close to the model prediction: Days 2, 10, 16, 19, and 20 August. Days 4 and 5 August have values somewhat less than the model and 6, 7, 12 and 21 August have values somewhat greater than the model. The profiles of λ_w/z_i, which

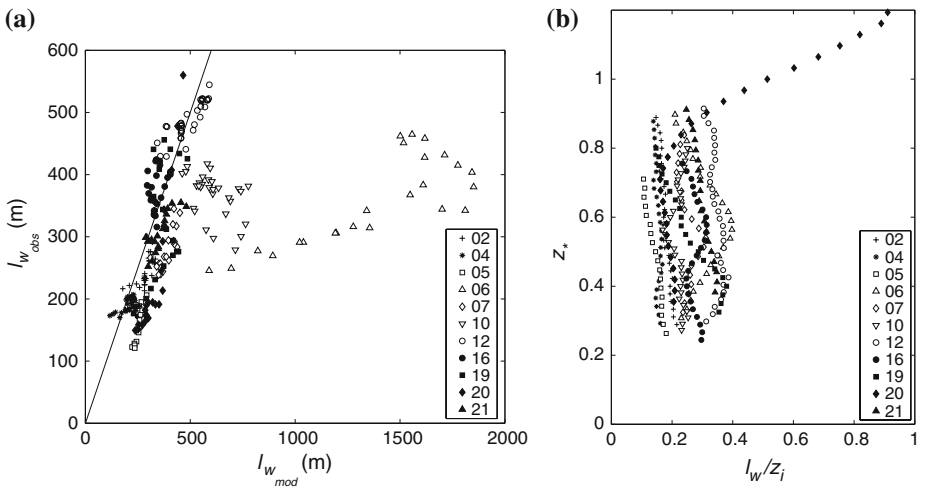

Fig. 6 **a** Comparison of the l_w estimates with the two methods: spectral fit (x-axis) or autocorrelation function (y-axis); **b** profiles of normalized along-wind integral scales estimated with the autocorrelation function of w

typically have values constant with height through many successive levels, demonstrate the repeatability of the peaks throughout much of the CBL, which is consistent with the measured vertical coherence being larger than predicted for isotropic turbulence using the observed integral length scale (Lothon et al. 2006).

The ratio l_w/z_i (Fig. 5b) is nearly constant or slightly decreasing with height in the region probed, but generally decreases close to z_i, likely due to the suppression of long-wavelength turbulence by the capping inversion. This was also found by Lothon et al. (2006), who used the autocorrelation function to estimate l_w. In Fig. 6a, we compare the estimates of l_w from the model fit and the autocorrelation function over the entire height range. They are close to each other except for 6 August. This case has a secondary peak at low wavenumber that becomes predominant in the middle of the CBL (Fig. 1), resulting in a greater increase in l_w in the model fit, compared to the autocorrelation estimate (Fig. 5b). We also show profiles of l_w/z_i obtained with the autocorrelation estimate (Lothon et al. 2006) in Fig. 6b. The deep aerosol-laden overlying layer on 20 August enabled us to estimate l_w through and above the inversion (Fig. 6b). The l_w profile for that case shows a sudden large increase with height starting around $z_* = 0.8$, likely due to wave activity above the inversion that is discussed below. We do not show this in Fig. 5b because the model does not fit spectra in the free troposphere.

6 Dissipation

Dissipation rates ϵ are estimated from the inertial subrange of the transverse velocity spectrum with Eq. 5 over a range $30 < kz_i < 80$. Figure 7 displays the profiles of ϵ normalized by the buoyancy term in the turbulence kinetic energy budget for all cases. We can see that they show significant scatter with $\overline{\epsilon} z_i / w_*^3 = 0.31 \pm 0.1$, where $\overline{\epsilon}$ is an average over all cases and height.

The large scatter in the dissipation profiles likely results from a combination of shear production near the surface and near the top of the CBL, and a varying ratio of entrainment

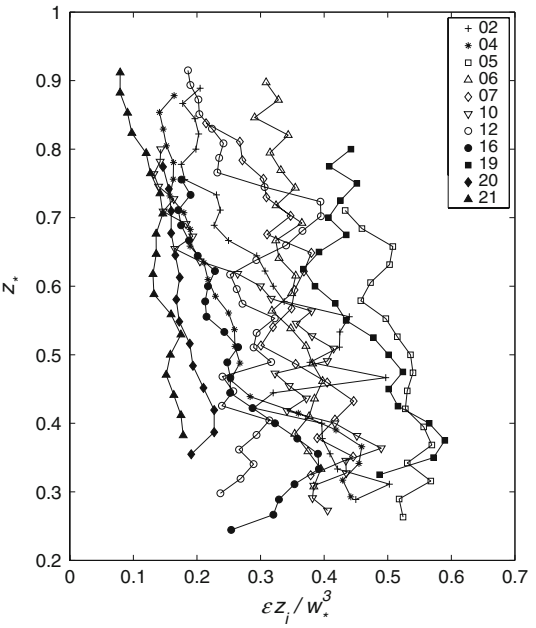

Fig. 7 Profiles of the normalized dissipation rate for each case

flux to surface buoyancy flux, defined as

$$A = \frac{-\langle w\theta_v \rangle_{z_i}}{\langle w\theta_v \rangle_0}, \tag{11}$$

where $\langle w\theta \rangle_{z_i}$ is the buoyancy flux at z_i and $\langle w\theta \rangle_0$ is the flux at the surface. We can use the normalized dissipation together with a model of the TKE budget to estimate A. For example, the TKE model of Lenschow (1974) reads,

$$D(z_*) = H(z_*) + S(z_*) + T_r(z_*), \tag{12}$$

where D, H, S and T_r are respectively dissipation, buoyancy and shear production, and transport (which includes the pressure term), normalized by the surface buoyancy flux. Lenschow (1974) derived an expression for $D(z_*)$, viz

$$D(z_*) = \langle H \rangle + \left(\frac{0.57}{\langle S \rangle + 3.75} \right) (\langle S \rangle - S) + S, \tag{13}$$

where variables in angle brackets are integrated and averaged over the entire CBL. Assuming a linear profile for H,

$$H(z_*) = 1 - (1 + A)z_*, \tag{14}$$

we have

$$\langle H \rangle = \frac{1 - A}{2}. \tag{15}$$

Lenschow (1974) used the Obukhov scaling expressions of Paulson (1970) and assumed that the momentum flux decreased linearly with height to zero at the CBL top, with the result that

$$S(z_*) = \left(\frac{-L}{z_i} \right) \frac{[1 - 15(z_i/L)z_*]^{-1/4}}{z_*}, \tag{16}$$

and

$$\langle S \rangle = \left(-\frac{L}{z_i} \right) \left[\ln \frac{z_i}{z_0} - \psi_1(x) \right], \tag{17}$$

where z_0 is the surface roughness length,

$$x = (1 - 15 z_i / L)^{1/4} \tag{18}$$

and

$$\psi_1(x) = 2 \ln \frac{1+x}{2} + \ln \frac{1+x^2}{2} - 2 \tan^{-1} x + \frac{\pi}{2}. \tag{19}$$

We use $z_0 = 0.11\,\mathrm{m}$, based on measurements by Hicks and Wesely (1981) over adjacent fields of soybeans and maize.

We also used the mixed-layer growth model of Tennekes (1973) and a parameterization from Mahrt and Lenschow (1976) for the contribution of shear production across the CBL top, but found that this contribution was negligible (smaller than 0.5% of the dissipation), so that we did not include it in our analysis. However, as discussed by Angevine (1999), the parameterization for shear production at the CBL top remains difficult. Substituting Eqs. 14, 15, 16 and 17 into (13), we can solve for the value of A that gives the best fit to the observed $\epsilon(z_*) z_i / w_*^3$ for each case. The values of A obtained are tabulated in Table 1; we find $A = 0.4$ on average, with a standard deviation of ± 0.2 over all the cases.

Shear at the surface contributed less than 1% of the dissipation for three very convective cases, between 2% and 20% for seven cases (10% to 20% for the days with largest mean wind speed), and about 35% for the anomalous 20 August case. This case had a high aerosol concentration layer above the CBL, possibly because this layer had earlier become detached from the CBL, which allowed us to observe considerable wave activity above the inversion that may have augmented the entrainment rate. The variance, for example, was about 50% of that in the CBL.

For two large wind speed cases (and small ζ), 5 and 19 August, $A < 0.2$, which seems surprising, since larger wind speeds within the PBL favour a greater production of turbulent energy by shear. Furthermore, this result does not agree with Kim et al. (2003), who found from large-eddy simulation that A increased from 0.13 to 0.3 as wind speed increased from 5 to $15\,\mathrm{m\,s^{-1}}$, with the surface buoyancy flux held constant. The two other cases with large mean wind (6 and 21 August) do have large A. The day 6 August is the case with significant spectral contribution at the mesoscale, possibly due to rolls, that may also contribute to the entrainment. Contrary to those cases, 5 and 19 August have smaller vertical coherence than other cases, according to Lothon et al. (2006), which may indicate less mesoscale organisation. Days 20 and 21 August are outliers, with $A = 0.7$, but Days 4, 20 and 21 August all show an overlying aerosol-laden layer with significant w variance and for one case (20 August), wave motion is observed, correlated with the motion within the CBL (see later in the text).

The average of $A = 0.4$ may seem large, since $A = 0.2$ or 0.25 has been widely used to parameterize the entrainment in bulk models. However, it is now accepted that larger entrainment is observed and modelled, especially with shear (Kim et al. 2003; Conzemius and Fedorovich 2007; Canut et al. 2009). $A = 0.2$ is a typical value for pure buoyancy-generated entrainment (Sullivan et al. 1998), and therefore we expect A to be larger in the presence of shear, or rolls or other mesoscale phenomena, or the occurrence of gravity waves in the overlying free troposphere. All these conditions are observed here among the various cases.

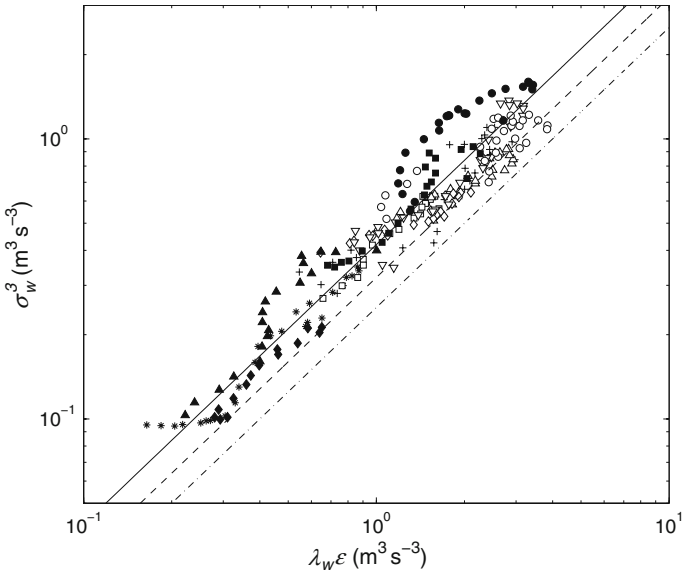

Fig. 8 σ_w^3 as a function of $\lambda_w \epsilon$ for all cases and at all levels between about $0.25 z_i$ and $0.9 z_i$. *Solid line* is a linear least-squares fit, *dashed line* is the theoretical slope for $\mu = 1$ and the *dashed-dotted line* for $\mu = 0.5$. *Symbols* for cases are the same as in Fig. 2

Figure 8 displays σ_w^3 as a function of $\epsilon \lambda_w$, where σ_w was first corrected for the effect of uncorrelated noise by using the variance at the first lag of the autocorrelation function of w (Lenschow et al. 2000). If μ were constant over height and over all cases, the data points should lie along a straight line, since the coefficient depends only on μ. This figure shows that, even if μ does vary, ϵ, λ_w and σ_w are still somewhat related in a simple manner. However, the best fit to the data points gives $b(\mu) = 0.42$ (with a regression coefficient of 0.96), which cannot be obtained with Eq. 7, since $b(\mu)$ reaches a maximum at $\mu \simeq 1.4$ ($b(1.4) = 0.33$). This implies that the KLKC model cannot predict the observed average coefficient that links these three variables. The fact that the fit to the observations lies above the lines predicted by Kaimal or von Kármán is consistent with the observed spectral energy increasing faster with wavenumber at low wavenumber than can be accounted for by the KLKC model.

Consistent with the variability of the spectra observed with height in the inertial subrange, ϵ decreases slightly with height in most cases and especially for the set of cases with low mean wind speed. This is surprising when considering the increasing contribution of shear to the production and dissipation of TKE close to surface with increasing wind. The two cases of the largest decrease of ϵ with height are 10 and 16 August, which have a wind maximum in the lower part of the CBL, consistent with decreasing dissipation. The relative contribution of shear at the top might be a factor, but the explanation is not straightforward from our analysis.

7 Behaviour of w Spectra at Small Wavenumbers

In the mixed layer, the inertial subrange spectral region of w can be collapsed onto a single curve by the normalization (Kaimal et al. 1976)

$$\frac{kS(k)}{w_*^2 \psi_\epsilon^{2/3}} = \frac{kS(k)}{(\epsilon z_i)^{2/3}} = \frac{4}{3} \alpha (k z_i)^{-2/3}, \tag{20}$$

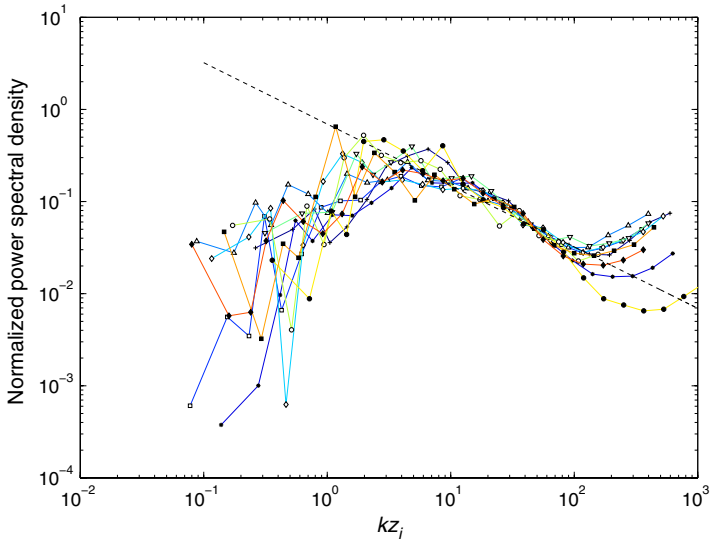

Fig. 9 Power spectral density of w multiplied by wavenumber and normalized by $w_*^2\psi_\epsilon^{2/3}$ ($kS(k)/(w_*^2\psi_\epsilon^{2/3})$) as a function of kz_i at $z_* = 0.35$ for the 11 cases. *Symbols* for cases are the same as in Fig. 2. *Dashed line* indicates the 2/3 slope

where

$$\psi_\epsilon = \frac{\epsilon z_i}{w_*^3}. \tag{21}$$

Since ϵ is determined from the spectrum in the inertial subrange, this collapses the observed spectra at the logarithmic mean of the inertial subrange. As shown in Fig. 9 for $z_* = 0.35$, some cases have a slope in the inertial subrange significantly steeper than the expected $-2/3$. We do not know why. Lothon et al. (2006) showed that beam averaging does not have a significant effect here.

Figure 10 displays averaged $\frac{kS(k)}{w_*^2\psi_\epsilon^{2/3}}$ for $kz_i \in [0.1, 1]$ over the entire probed depth as a function of shear across the CBL top. The shear is calculated using the UHF profiler data with the profiler collocated with the HRDL lidar, as well as at Sadorus, 5 km away, for cases for which there were no data from the collocated profiler (2, 7, 20 and 21 August) due to instrumental issues. Figure 10 shows a tendency for less energy at small wavenumbers as the shear increases. However, the limited number of cases on which this is based (only two cases with large shear—6 and 20 August) makes this only a tentative conclusion.

One possibility for why this may be the case is suggested by the large-eddy simulation results of Conzemius and Fedorovich (2006, 2007), who found that the bulk Richardson number Ri_b is approximately constant within the entrainment zone. To maintain Ri_b constant, larger shear must be associated with a larger jump in virtual potential temperature $\Delta\theta_v$, which may retard wave propagation through the entrainment zone.

To lend support to this suggestion, we plotted $\Delta\theta_v$ versus shear in Fig. 11. Due to the complexity and uncertainty of determining the entrainment zone, we estimated shear from UHF profiler observations as the difference between the horizontal wind components at $z = z_i + z_i/10$ and the mean of the wind components within the CBL. $\Delta\theta_v$ was estimated from the rawinsondes launched about 5 km from the lidar site. We then estimated the bulk

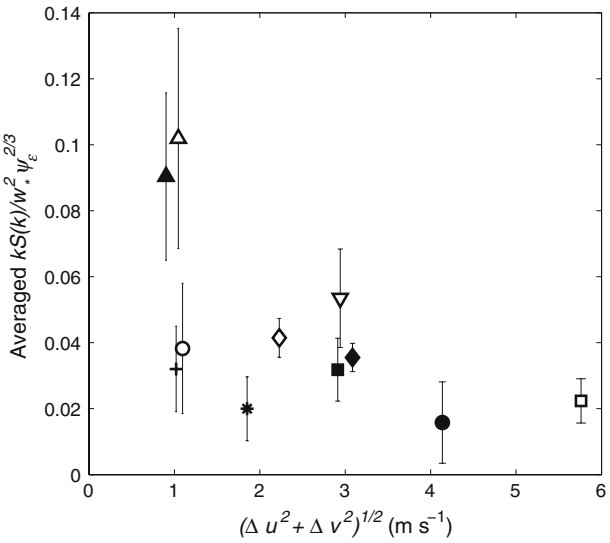

Fig. 10 Averaged value of $\frac{kS(k)}{w_*^2\psi_\epsilon^{2/3}}$ for $kz_i \in [0.1, 1]$ and over the entire probed depth as a function of $\sqrt{\Delta u^2 + \Delta v^2}$, averaged over the considered time period (Δu and Δv are the differences in wind components u and v between just above the CBL top ($z = z_i + z_i/10$) and their average within the depth of the CBL). *Symbols* for cases are the same as in Fig. 2. *Error bars* indicate the standard deviation over the probed CBL depth

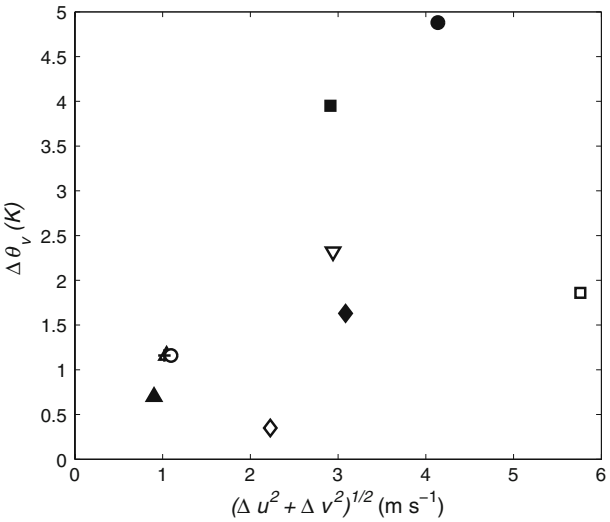

Fig. 11 Jump in virtual potential temperature as a function of shear. *Symbols* for cases are the same as in Fig. 2

Richardson number as

$$Ri_b = \left(\frac{g}{T_v}\right)\frac{\Delta\theta_v \Delta z}{\Delta u^2 + \Delta v^2}, \tag{22}$$

with $\Delta z = 2z_i/10$.

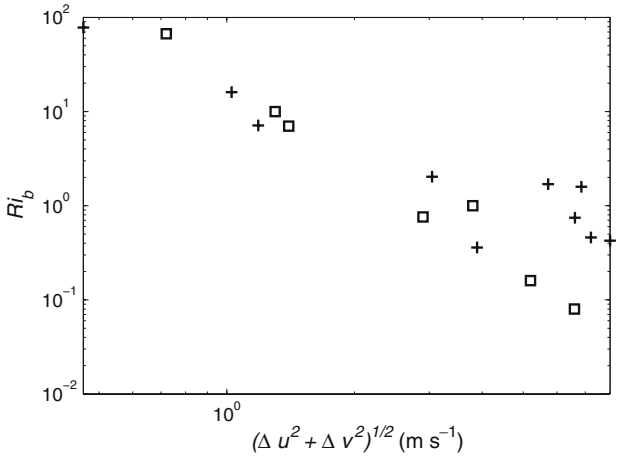

Fig. 12 Observed bulk Richardson number versus shear across the CBL top during the 11 LIFT cases ('*plus sign*') and during FLATLAND cases ('*open square*', after Angevine 1999)

Contrary to Conzemius and Fedorovich (2006), we find that Ri_b varies from case to case, with estimates in agreement with Angevine (1999). We point out, however, that Ri_b cannot be easily estimated within the entrainment zone, but only across it. Also, there is a large uncertainty in the estimated Ri_b. Despite this, Fig. 12 shows that our estimates agree well with the independent estimates of Angevine (1999), which is promising. The difference between the two estimates lies in the fact that our estimates level out at large shear, which is what we would expect, since Ri_b should tend to become constant around the Kelvin-Helmoltz instability limit.

8 Discussion of Specific Cases

To illustrate the variability of CBL structure among the 11 cases, we show height-time cross-sections of backscatter and Doppler velocity measured by the HRDL for three cases with quite different structures. These differences are manifested in measurements of aerosols, cumulus cloud base, and vertical velocity. The w spectra for these cases are shown in Fig. 1.

8.1 6 August 1996

Figure 13 shows an example with large mean CBL wind speed and large u_*, but small shear across the top and small ζ. This case has the largest λ_w/z_i likely due to mesoscale motions within the CBL and has the smallest μ of all the cases. The cloud cover is 20% and it is a potential longitudinal roll day since $\zeta < 25$ (Weckwerth 1999).

8.2 12 August 1996

Figure 14 shows an interesting case of regularly-spaced similarly-shaped thermals systematically capped by cumulus clouds (Fig. 14) with 41% cloud cover. As mentioned previously, l_w is linked more to the size of the eddies and λ_w to the space between thermals (3 to 4 km). The latter is responsible for the clear peak in the w spectra (Fig. 1e). The spectra, which in

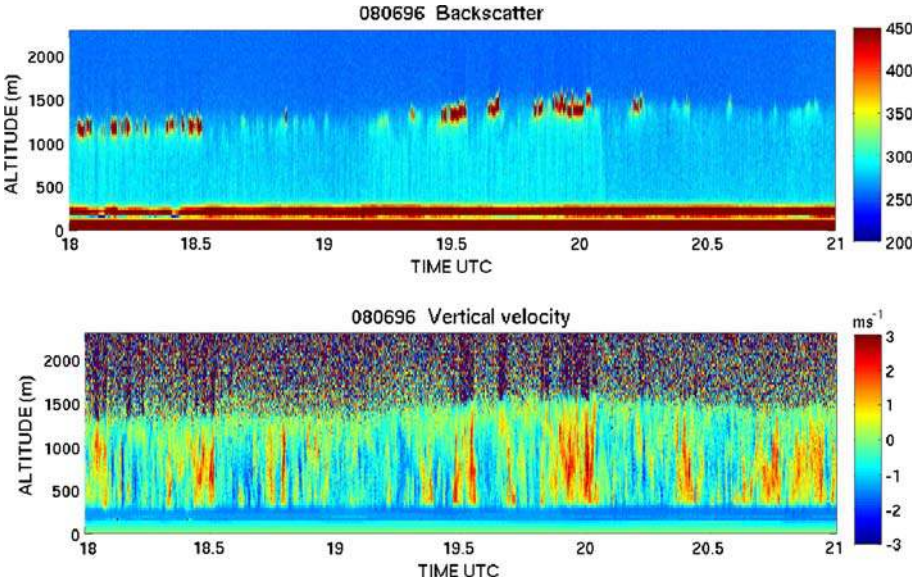

Fig. 13 Backscatter (*top panel*) and w (*bottom panel*) observed by the lidar on 6 August. This case has large mesoscale contributions to the spectra

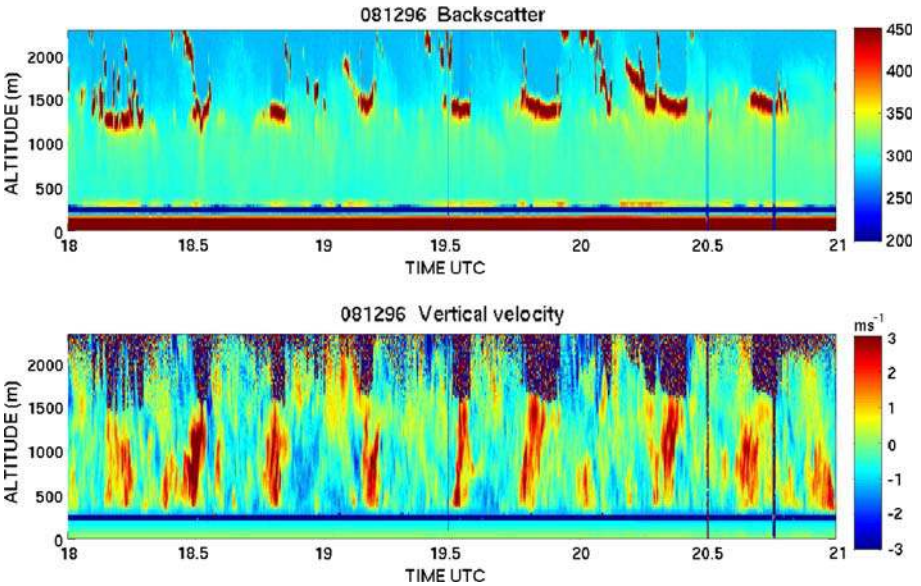

Fig. 14 Backscatter (*top panel*) and w (*bottom panel*) observed by the lidar on 12 August. This case shows an organized response to cumulus clouds

this case have almost no high-wavenumber noise, also have a slope in the inertial subrange that is very close to the theoretical $-2/3$. The maximum backscatter is at cloud base and thus is easily detected. However, the lidar pulse is strongly attenuated within the clouds, so that we cannot estimate their depth or shape. The regular spacing between clouds suggest some

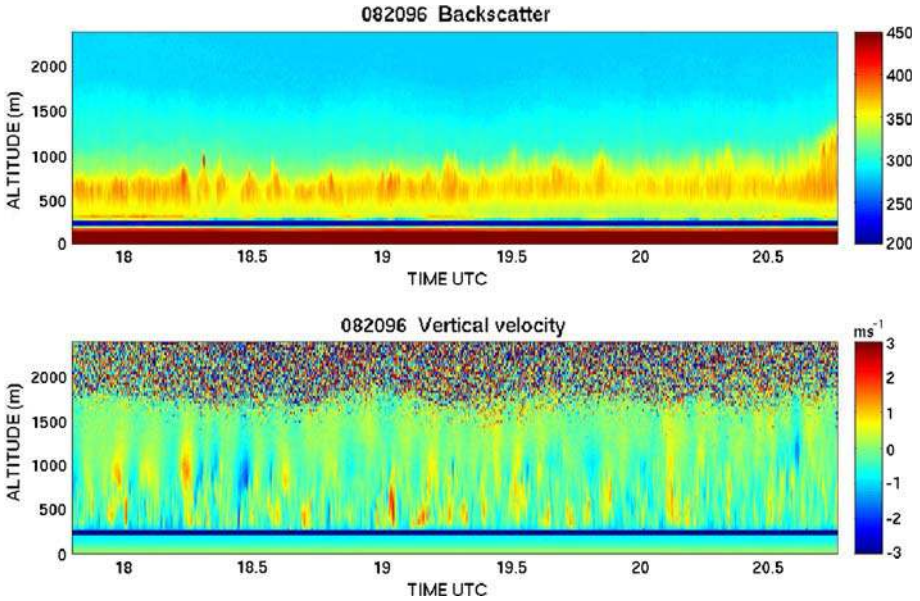

Fig. 15 Backscatter (*top panel*) and w (*bottom panel*) observed by the lidar on 20 August. This case shows a wave response above the CBL

sort of coherent cellular structure. It is unlikely to be rolls since $\zeta > 25$ and cloud streets are normally approximately aligned with the mean wind, especially in a no-shear case such as this. We suspect that the separation distance observed here may be more the result of cloud suppression in the cloud periphery due to downdrafts. This case and that of 16 August were the only two cases showing such a sharp spectral peak throughout the probed CBL depth (Fig. 1e), and characterized by a rapid decrease in energy at low wavenumbers. They are significantly different from spectra proposed in the literature. The two cases have similar w_*, l_w, and λ_w, although both ζ and Ri_b differ.

8.3 20 August 1996

Figure 15 shows a special case among the 11 days. On this day there was sufficient aerosol above the CBL and z_i was small enough that the lidar detected backscatter and thus could measure w well into the lower free troposphere. No clouds were observed. Figure 15 shows that the lidar identified clear evidence of waves in this overlying layer. Figure 16 shows w spectra at $z_i/2$, z_i and $1.3z_i$, and at $1.3z_i$ we observe a peak at $\lambda = 3$ km that remains very significant at $z = z_i$, and seems to still be present within the CBL despite being mostly masked by turbulence. The l_w profile for this case (Fig. 5a) shows a rapid increase starting from $z = 0.8z_i$, due to the larger scale associated with the wave above the CBL. The waves in the free troposphere also appear to be correlated with the vertical motion within the CBL at the same wavenumber. An overlying aerosol-laden layer was similarly observed in other cases, especially 4 and 21 August, with significant vertical velocity variance but with no clear evidence of wave motion.

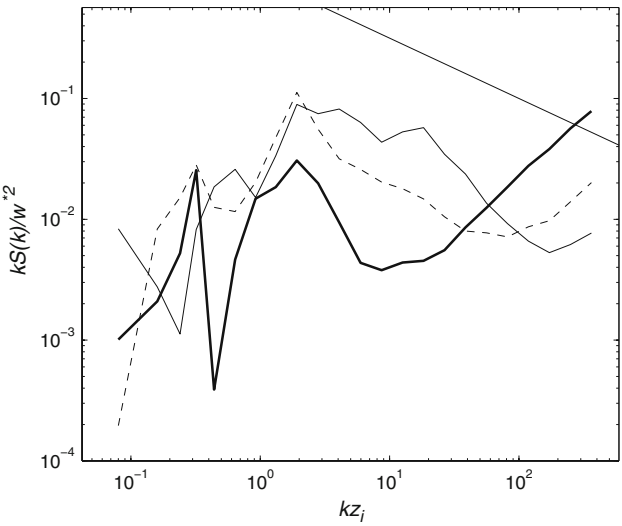

Fig. 16 w spectrum at three different levels on 20 August: (*solid thin line*) in the mixed layer ($z = z_i/2$), (*dashed line*) at the CBL top ($z = z_i$) and (*solid thick line*) in the overlying wave layer ($z = 1.3z_i$)

9 Concluding Remarks

The w spectra observed with the HRDL throughout the mixed layer revealed a significant continuity of spectral peaks throughout the depth of the CBL. This is consistent with the large coherence in the vertical direction found by Lothon et al. (2006). The spectra also showed large case-to-case variability, both in the location of the spectral maximum, and in the spectral shape in the energy-containing region.

We used the KLKC model as a basis for comparison with the measured spectra. This model uses the integral scale and a parameter μ that governs the curvature of the spectrum over the transition between the inertial subrange and the energy-containing scales. We find that the spectra are more peaked than predicted by the Kaimal ($\mu = 0.5$) spectra; and at least as peaked as the von Kármán ($\mu = 1$) spectra. The Højstrup (1982) model, which was developed for the lower part of the CBL, generally overestimates the spectral energy.

The large case-to-case variability makes it difficult to develop a simple universal model of the w spectra in the CBL, and indeed, we found that existing models do not characterize the w spectra very well. We also found that: (i) in general, the spectra become less sharp with increasing height for $z_* < 0.7$; (ii) cases with the largest mean wind speed have decreasing peak wavelength with height and flatter spectra; (iii) for the most convective cases, the wavelength of maximum energy remains constant with height and the spectra are steeper; (iv) the larger the cloud fraction, the higher the level at which the flattest spectrum occurs within the CBL, likely due to low wavenumber contributions to the spectrum from cloud activity.

We also find a large case-to-case variability of our estimates of normalized dissipation deduced from the spectra, likely due for the most part to a varying ratio of entrainment flux to surface flux.

Finally, we find a larger contribution at low wavenumbers for smaller shear across the inversion, which we hypothesize is a result of differences in dynamical processes associated with inversion strength.

The dead zone of the HRDL was a significant limitation in our study. Therefore, we suggest that, in operations consideration be given to pointing the HRDL horizontally, with a mirror located a few hundred metres away, that would redirect the beam upward and eliminate the dead-zone. Increasing the sensitivity of the lidar would allow observation across the inversion. With these two improvements, a similar analysis of w statistics could be obtained throughout the entire depth of the CBL.

Acknowledgements The National Center for Atmospheric Research (NCAR) is sponsored by the National Science Fundation. The LIFT project was funded by the NCAR Atmospheric Technology Division Director's Office and the Department of Energy/OAGR. This work was made possible thanks to MMM and EOL Divisions of NCAR. The authors would like to thank Wayne Angevine and three anonymous reviewers for their useful comments.

References

Angevine WM (1999) Entrainment results including advection and case studies from the Flatland boundary layer experiments. J Geophys Res 104:30,947–30,963

Angevine WM, Grimsdell AW, Hartten LM, Delany AC (1998) The Flatland boundary layer experiments. Bull Am Meteorol Soc 79:419–431

Banakh VA, Smalikho IN (1999) Measurements of turbulent energy dissipation rate with a CW Doppler lidar in the atmospheric boundary layer. J Atmos Ocean Technol 16:1044–1061

Canut G, Lothon M, Said F (2009) Observation of entrainment at the interface between monsoon flow and Saharan Air Layer. Q J Roy Meteorol Soc (in press)

Caughey SJ, Palmer SG (1979) Some aspects of turbulence structure through the depth of the convective boundary layer. Q J Roy Meteorol Soc 105:811–827

Cohn SA, Angevine WM (2000) Boundary layer height and entrainment zone thickness measured by lidars and wind-profiling radars. J Appl Meteorol 39:1233–1247

Cohn SA, Mayor SD, Grund TM, Weckwerth TM, Sneff C (1998) The Lidars in Flat Terrain experiment LIFT. Bull Amer Meteorol Soc 79:1329–1343

Conzemius RJ, Fedorovich E (2006) Dynamics of sheared convective boundary layer entrainment. Part I: methodology background and large-eddy simulations. J Atmos Sci 63:1151–1178

Conzemius RJ, Fedorovich E (2007) Bulk models of the sheared convective boundary layer: Evaluation through large eddy simulations. J Atmos Sci 64:786–807

Emeis S, Schafer K, Munkel C (2008) Surface-based remote sensing of the mixing-layer height—a review. Meteorol Z 17:621–630

Grimsdell AW, Angevine WM (1998) Convective boundary layer height measurement with wind profilers and comparison to cloud base. J Atmos Oceanic Technol 15:1331–1338

Grimsdell AW, Angevine WM (2002) Observations of the afternoon transition of the convective boundary layer. J Appl Meteorol 41:3–11

Grund CJ, Banta RM, George JL, Howell JN, Post MJ, Richter RA, Weickman AM (2001) High-resolution Doppler lidar for boundary layer and cloud research. J Atmos Oceanic Technol 18:376

Hageli P, Steyn DG, Strawbridge KB (2000) Spatial and temporal variability of mixed-layer depth and entrainment zone thickness. Boundary-Layer Meteorol 97:47–71

Hicks BB, Wesely ML (1981) Heat and momentum transfer characteristics of adjacent fields of soybeans and maize. Boundary-Layer Meteorol 20:175–185

Hogstrom U (1996) Review of some basic characteristics of the atmospheric surface layer. Boundary-Layer Meteorol 78:215–246

Højstrup J (1982) Velocity spectra in the unstable planetary boundary layer. J Atmos Sci 39:2239–2248

Kaimal JC, Wyngaard JC, Coté OR (1972) Spectral characteristics of surface layer turbulence. Q J Roy Meteorol Soc 98:653–689

Kaimal JC, Wyngaard JC, Haugen DA, Coté OR, Izumi Y (1976) Turbulence structure in the convective boundary layer. J Atmos Sci 33:2152–2169

Kaimal JC, Eversole RA, Lenschow DH (1982) Spectral characteristics of the convective boundary-layer over uneven terrain. J Atmos Sci 39:1098–1114

Kàrmàn TV (1948) Progress in the statistical theory of turbulence. Proc Nat Akad Sci 34:530–539
Katul G, Chu C-R (1998) A theoretical and experimental investigation of energy-containing scales in the dynamic sublayer of boundary-layer flows. Boundary-Layer Meteorol 86:279–312
Kim S, Park S, Moeng CH (2003) Entrainment processes in the convective boundary layer with varying wind shear. Boundary-Layer Meteorol 108:221–245
Kristensen L, Lenschow DH, Kirkegaard P, Courtney M (1989) The spectral velocity tensor for homogeneous boundary layer turbulence. Boundary-Layer Meteorol 47:149–193
Lammert A, Boesenberg J (2006) Determination of the convective boundary-layer height with laser remote sensing. Boundary-Layer Meteorol 119:159–170
Lenschow DH (1974) Model of the height variation of the turbulence kinetic energy budget in the unstable planetary boundary layer. J Atmos Sci 31:465–474
Lenschow DH, Stankov BB (1986) Length scales in the convective boundary layer. J Atmos Sci 43:1198–1209
Lenschow DH, Wulfmeyer V, Senff C (2000) Measuring second- through fourth-order moments in noisy data. J Atmos Ocean Technol 17:1330–1347
Lothon M, Lenschow DH, Mayor S (2006) Coherence and scale of vertical velocity in the convective boundary-layer. Boundary-Layer Meteorol 121:521–536
Mahrt L, Lenschow DH (1976) Growth dynamics of the convective mixed layer. J Atmos Sci 33:41–51
Mann J (1994) The spatial structure of neutral atmospheric surface-layer turbulence. J Fluid Mech 273:141–168
Martucci G, Matthey R, Mitev V, Richner H (2007) Comparison between backscatter lidar and radiosonde measurements of the diurnal and nocturnal stratification in the lower troposphere. J Atmos Oceanic Technol 24:1231–1244
Militzer JM, Michaelis MC, Semmer SR, Norris KS, Horst TW, Oncley SP, Delany AC, Brock FV (1995) Development of the prototype PAMIII/Flux-PAM surface meteorological station. In: Proceedings of the 9th symposium on meteorological observations and instrumentation, American Meteorological Society, Boston, pp 490–494
Paulson CA (1970) The mathematical representation of wind speed and temperature profiles in the unstable atmospheric boundary layer. J Appl Meterol 9:857–861
Sullivan PP, Moeng CH, Stevens B, Lenschow DH, Mayor SD (1998) Structure of the entrainment zone capping the convective atmospheric boundary layer. J Atmos Sci 55:3042–3064
Tennekes H (1973) A model for the dynamics of the inversion above a convective boundary layer. J Atmos Sci 30:538–567
Weckwerth T (1999) An observational study of the evolution of horizontal convective rolls. Mon Weather Rev 127:2160–2179
White AB, Senff CJ, Banta RM (1999) A comparison of mixing depths observed by ground-based wind profilers and an airborne lidar. J Atmos Oceanic Technol 16:584–590
Wilczak JM, Gossard EE, Neff WD, Eberhard WL (1996) Ground-based remote sensing of the atmospheric boundary layer: 25 years of progress. Boundary-Layer Meteorol 78:321–349